Exploiting Ru-Induced Lattice Strain in CoRu Nanoalloys for Robust Bifunctional Hydrogen Production

Weidong Li[a,b], Yuanxuan Zhao[c], Yuan Liu[a], Mingzi Sun[d], Geoffrey I. N. Waterhouse[e], Bolong Huang[d]*, Kan Zhangf, Tierui Zhangg, Siyu Lu [a]*

[a] Green Catalysis Center, and College of Chemistry, Zhengzhou University, Zhengzhou 450001, China

[b] College of Materials Engineering, Henan International Joint Laboratory of Rare Earth Composite Material, Henan University of Engineering, Zhengzhou, 451191 China

[c] Key Laboratory of Photochemical Conversion and Optoelectronic Materials, Technical Institute of Physics and Chemistry, Chinese Academy of Sciences, Beijing, 100190 China

[d] Department of Applied Biology and Chemical Technology, The Hong Kong Polytechnic University, Hung Hom, Kowloon, Hong Kong SAR, China

[e] School of Chemical Sciences, The University of Auckland, Auckland, 1142 New Zealand

[f] MIIT Key Laboratory of Advanced Display Material and Devices, School of Materials Science and Engineering, Nanjing University of Science and Technology, Nanjing, 210094 China

[g] Key Laboratory of Photochemical Conversion and Optoelectronic Materials, Technical Institute of Physics and Chemistry, Chinese Academy of Sciences, Beijing, 100190 China

* The corresponding author.

E-mail: sylu2013@zzu.edu.cn, bhuang@polyu.edu.hk

Abstract

Designing bifunctional catalysts capable of driving the electrochemical hydrogen evolution reaction (HER) and also H_2 evolution via the hydrolysis of hydrogen storage materials such as ammonia borane (AB) is of considerable practical importance for

future hydrogen economies. Herein, we systematically examined the effect of tensile lattice strain in CoRu nanoalloys supported on carbon quantum dots (CoRu/CQDs) on hydrogen generation by HER and AB hydrolysis. By varying the Ru content, the lattice parameters and Ru-induced lattice strain in the CoRu nanoalloys could be tuned. The $CoRu_{0.5}$/CQDs catalyst with an ultra-low Ru content (1.33 wt.%) exhibited excellent catalytic activity for HER (η=18 mV at 10 mA cm^{-2} in 1 M KOH) and extraordinary activity for the hydrolysis of AB with a turnover frequency of 3255.4 $mol_{(H2)}\ mol^{-1}_{(Ru)}\ min^{-1}$ or 814.7 $mol_{(H2)}\ mol^{-1}_{(cat)}\ min^{-1}$ at 298 K, respectively, representing one of the best activities yet reported for AB hydrolysis over a ruthenium alloy catalyst. Moreover, the $CoRu_{0.5}$/CQDs catalyst displayed excellent stability during each reaction, including seven alternating cycles of HER and AB hydrolysis. Theoretical calculations revealed that the remarkable catalytic performance of $CoRu_{0.5}$/CQDs resulted from the optimal alloy electronic structure realized by incorporating small amounts of Ru, which enabled fast interfacial electron transfer to intermediates, thus benefitting H_2 evolution kinetics. Results support the development of new and improved catalysts HER and AB hydrolysis.

Introduction

Hydrogen is one of the best environmentally friendly fuels and a promising efficient energy carrier for future applications because of its clean, abundance, high energy density, and renewability. Thus, exploring sustainable and efficient hydrogen produce strategy is urgently needed. At present, the two most promising ways to produce it cleanly and efficiently for industrial use are electrochemical water splitting and decomposition of readily available hydrogen storage chemicals such as ammonia borane (NH_3BH_3, H content up to 19.6 wt%, non-toxicity, and superior stability in aqueous solutions). Although these methods give people the option to avoid using fossil fuels, additional catalyst input also faces severe challenges. It is well known, platinum is generally considered to be the best catalyst for both HER and AB hydrolysis. However, their expensiveness and scarcity limit their large-scale industrial application. Therefore, it is of great significance to explore inexpensive alternatives for Pt catalysts.

Strain regulation has been widely investigated to control the interatomic distances, and thus alter the electronic and geometrical structure of the active sites to optimize the electrocatalytic activities. For the Pt-based bimetallic catalytic systems, the structure-

relevant strain effect has been used to tune the catalytic reactivity. Traditionally reported strain effect is generated by compressing or expanding the nanostructure to modify the atomic arrangement of the surface layer. The strain effect at the atomic scale can lead to the change in lattice parameter, and the electroactivity. In spite of these improvements in electrocatalysis achieved through strain regulation in recent years, they are rarely been applied in ruthenium-based catalyst modification for HER.

Recently, the transition metal (TM) carbides, nitrides, sulfides, phosphides, borides have been widely used in hydrogen evolution reaction. Nevertheless, their catalytic activity is unable to catch up with Pt-based catalysts. In this view, more and more attention has been paid to study noble metals and transition metals alloy compounds. By incorporating TMs, not only the catalyst cost decreases, but the lattice deformation occurs due to the difference in atomic radius, which can observably improve the catalysis performance. As an earth-abundant and low-cost metal, monometallic Co is known to be poor HER catalysts because their hydrogen binding energy (HBE) values are too weak. However, ruthenium is regarded as a promising HER electrocatalyst in alkaline media due to the fast water dissociation process. However, the interaction between Ru and H atoms is usually too strong and the induced overbinding effect lowers the efficiency ofthe subsequent hydrogen desorption process. By alloying Co with Ru, the incorporation of Ru atoms in the Co matrix balances the H binding strength, which promotes water adsorption/activation and optimizes H adsorption/desorption. On other hand, the incorporation of Ru with a mismatch lattice constant also inevitably induces the lattice strain to significantly improve the catalytic efficiency. Moreover, previous studies have suggested that the d-band center of noble metals can be modulated by lattice strain, which can appreciably optimize the bonding with reaction intermediates. Hence, applying lattice strain by metal alloy strategy is a powerful method to the geometrical and electronic structure of the active sites and further improvesthe catalytic activities. （这里顺序调整了一下）

In comparison with CNTs, GO, g-C_3N_4, MOFs and other carbonaceous materials, carbon quantum dots (CQDs) have the advantages of the simple synthesis processby an environmentally friendly, low-cost, heteroatomic dopping and high-yield way. More importantly, the abundant functional groups (-OH, -COOH, -NH_2, etc.) at CQDs surfaces not only provide favorable active sites but also anchor the metal-precursors to prevent the aggregation, which enable the materials engineering of multicomponent catalysts. In view of their near-ideal properties, combining metal nanoparticles with

CQDs offers a promising route to developing efficient metal/carbon hybrid catalysts.（老师，这一段删掉是否更合适？）

In this work, we report a simple and effective synthesis method for the preparation of $CoRu_x$ nanoalloy on carbon quantum dots loaded ($CoRu_x$/CQDs) catalysts with intrinsic lattie by adjusting the content of Ru. Significantly, $CoRu_{0.5}$/CQDs not only afford extraordinary catalytic activity for the hydrogen evolution reaction (HER) with extremely low overpotentials in alkaline solution (η = 18 mV @ 10 mA cm^{-2} in 1.0 M KOH) but also shows the outstanding activity for chemical hydrogen generation from the hydrolysis of ammonia borane (AB) with a high turnover frequency (TOF) of 3255.4 mol (H_2) $mol^{-1}_{(Ru)}$ min^{-1} and 814.7 mol (H_2) $mol^{-1}_{(cat)}$ min^{-1} at 298 K. Furthermore, the $CoRu_{0.5}$/CQDs demonstrates strong stability for both HER and AB hydrolysis after alternating 7 cycles. These benefits allow this catalyst to be used in multi-reactions with greatly increased efficiency of practical hydrogen production. These impressive catalytic performances are comparable to or even better than those of state-of-the-art catalysts. As revealed by a series of spectroscopic and theoretical calculations analysis, the excellent catalytic performance of the $CoRu_{0.5}$/CQDs results from the effective electronic coupling of Co and Ru, in which the introduction of Ru dominates the dissociation of H_2O in the alkaline condition while the generation of H_2 is further facilitated by the Co. .

Results and discussion

The high-purity CQDs were synthesized by a typical one-step hydrothermal method at 200 °C for 4 h. The morphology of the CQDs was examined by transmission electron microscopy (TEM, Fig. S1 Supporting information). The X-ray diffraction (XRD, Fig. S2) showed a broad peak at 22.40° which associated with a graphite structure. The Fourier-transfer infrared (FT-IR, Fig. S3) and X-photoelectron spectroscopy (XPS, Fig. S4) intensively suggested that the surface of the as-prepared CQDs was passivated by both oxygen and nitrogen-containing groups. The CQDs solution exhibited distinctly blue-green fluorescence with a maximum peak at 505 nm upon 440 nm excitation(Fig. S5). The UV–vis absorption spectrum (Fig. S5) exhibits two excitonic absorption bands at about 275 and 325 nm, which were assigned to the $\pi \rightarrow \pi^*$ transition of the aromatic domains and $n \rightarrow \pi^*$ transitions between the oxygen-/nitrogen containing groups and sp^2 domains, respectively.

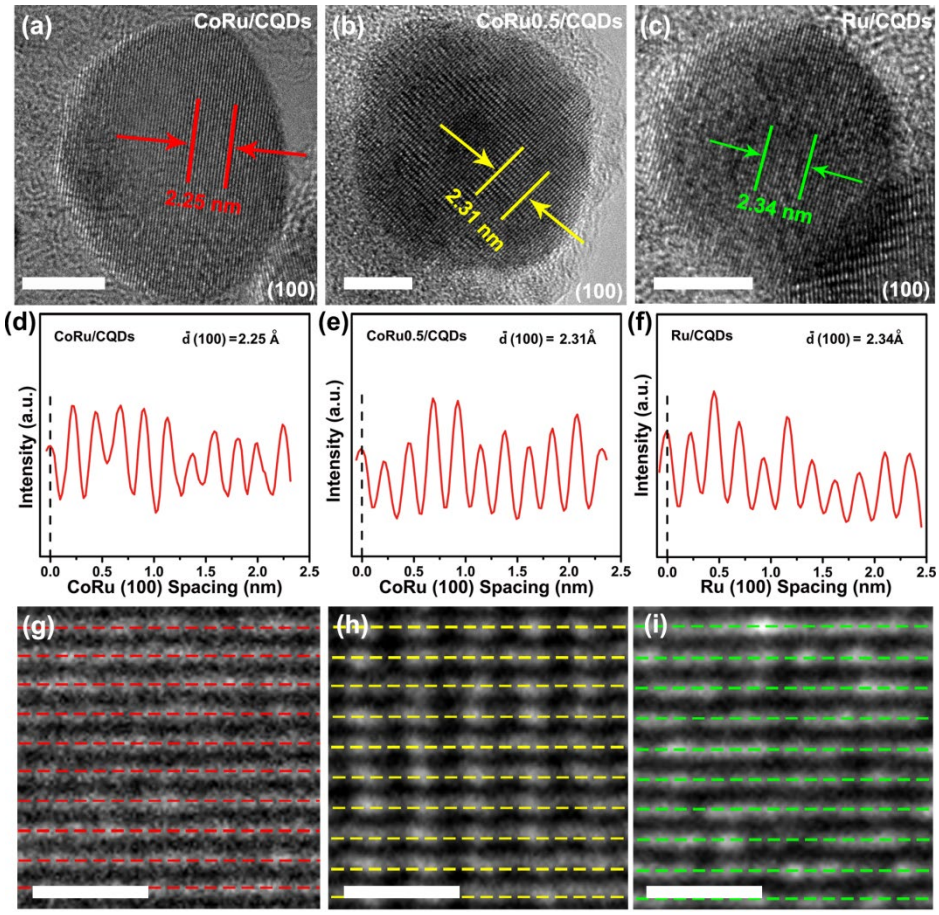

Fig. 1 a-c) HRTEM image of CoRu/CQDs, $CoRu_{0.5}$/CQDs, Ru/CQDs. scale bar: 5 nm. d-f) The integrated pixel intensities for the CoRu/CQDs, $CoRu_{0.5}$/CQDs and Ru/CQDs lattices as selected in a to c, respectively. g-i) A direct evidence of tensile strain with the aligned the ten atomic layers on the top of CoRu/CQDs, $CoRu_{0.5}$/CQDs, Ru/CQDs. scale bar: 1 nm.

Benefiting from their small size, strong coordination ability, and unique electron transfer abilities, the CQDs were expected to serve as a nanosized template to control the growth and crystallization of metal alloy nanoparticles (NP), engineering the morphology and interface of catalyst. Subsequently, we have synthesized a series of hybrid $CoRu_x$/CQDs materials with different ruthenium content from the hydrothermal reaction of $RuCl_3$, $Co(NO_3)_2$, and CQDs at 200 °C for 8 h. The accurate molar ratio of Co to Ru in the final product was confirmed by inductively coupled plasma-optical emission spectrometer (ICP-OES) (Table S1). Thus, the samples were denoted as CoRu/CQDs, $CoRu_{0.7}$/CQDs, $CoRu_{0.5}$/CQDs, $CoRu_{0.3}$/CQDs and $CoRu_{0.1}$/CQDs.

The related XRD patterns were first presented in Fig. S6. Similar diffraction features of a broad and weak peak of C (002) were detected, confirming the existence of carbon layers. Besides, with the increase of Ru content, the diffraction peak gradually moved from hcp-structured Ru (JCPDS-89-4903) to hcp-structured CoRu (JCPDS-65-

8976), indicating the lattice constant has changed.

The morphology of the as-prepared $CoRu_{0.5}$/CQDs hybrid was observed with transmission electron microscopy (TEM). As shown in Fig. S7, uniform products were clearly composed of CoRu alloy particles loaded in N-doped graphene layers and interconnected via graphitic carbon layers. High-resolution TEM was used to determine the amount of strain on different sites of CoRu/CQDs, $CoRu_{0.5}$/CQDs and Ru/CQDs. We focus on the (100) direction in the zone axis as a representative facet for studying the lattice strain. Then we examined the central regions of the CoRu/CQDs, $CoRu_{0.5}$/CQDs, and Ru/CQDs and obtained the averaged (100) facet spacing over ten atomic layers (Fig. 1 a-c), avoiding possible surface defects as well as blurry boundaries. The integrated pixel intensities were shown in Fig. 1 d-f, for the CoRu/CQDs, CoRu0.5/CQDs, and Ru/CQDs lattices as selected in Fig. 1, a-c, respectively. The averaged CoRu (100) spacing in CoRu/CQDs and Ru (100) spacing in Ru/CQDs were 2.25 Å and 2.34 Å, respectively, which agreed well with hcp-structured CoRu (JCPDS-65-8976) hcp-structured Ru (JCPDS-89-4903) and previously reported lattice constants. The intensity profile of CoRu (100) spacing in $CoRu_{0.5}$/CQDs in Fig. 1e suggested a much bigger lattice distance compared with that of the pristine CoRu, with an averaged spacing of 2.31 Å, which represents a slight tensile strain after the introduction of Ru with larger atomic radius. This phenomenon can be explained by a possible inhomogeneity of the Ru concentration near the Co surface and within the bulk during the pyrolysis processes. The surfaces may have a higher concentration of Ru and thus lead to larger structural changes. To have an intuitive understanding of how much the tensile lattice strain is, we aligned the (100) atomic layers on the top in Fig. 1 g-i. After ten layers of accumulation in spacing differences, the bottom layer of tensile CoRu in $CoRu_{0.5}$/CQDs was much lower position than that of the CoRu in CoRu/CQDs, offering direct evidence of the lattice tensile. We have measured the lattice changes of different particles, as shown in Fig. S8, the successful observation of tensile strain in the CoRu (100) facet, further demonstrating the existence of lattice strain introduced by the Ru.

The composition and degree of graphitization of the as-synthesized samples were further revealed by Raman spectroscopy. As shown in Fig S9, the Raman spectra identified typical D (~1340 cm^{-1}) and G (1572 cm^{-1}) bands and 2D bands at around 2703 cm^{-1}. The relative intensity (ID/IG) ratios of CoRu/CQDs, $CoRu_{0.7}$/CQDs, $CoRu_{0.5}$/CQDs, $CoRu_{0.3}$/CQDs and $CoRu_{0.1}$/CQDs were calculated to be 0.97, 0.98, 1.09, 0.95, 0.95, respectively, indicated the large amounts of defects in the samples. The

highest intensity ratio of $CoRu_{0.5}$/CQDs indicates an increase in structural defects, suggesting that the local lattice strain gave rise to structural defects by the appropriate Co/Ru ratio. The FT-IR spectra (Fig. S10) indicated the formation of polyaromatic structures and the presence of nitrogen-containing groups along with the CQDs. The specific surface area and pore size distribution were obtained by N_2 adsorption/desorption isotherms. As expected in Fig. S11, the CoRu0.5/CQDs possessed a high Brunauer–Emmett–Teller (BET) specific surface area of 332.9 $m^2 g^{-1}$. with an average nanopore size of ca. 4.7 nm. The high specific surface area accelerate the charge transfer with the more active sites, which benefits theelectro-chemical processes.

To investigate the chemical states of the as-prepared sample, the X-ray photoelectron spectroscopy (XPS) analysis was applied to the $CoRu_{0.5}$/CQDs. The XPS survey spectra showed that the surface of $CoRu_{0.5}$/CQDs was mainly composed of elemental C, N, O, Co, and Ru (Fig. S12). To explore the evolution trends of the electronic structures for Co and Ru, the XPS spectra for $CoRu_x$/CQDs were further analyzed and placed together with that of Co/CQDs and Ru/CQDs for comparison. Fig. 2a showed the Co 2p high-resolution spectra of $CoRu_x$/CQDs and Co/CQDs. The Co 2p peaks gradually shift to higher binding energy with increasing Ru content, indicating a slight variation of surface electronic structures in the nanoalloys. Meanwhile, the Ru 3p peaks of the $CoRu_x$/CQDs show a negative shift compared to that of pure Ru (Fig. 2b), which is ascribed to the efficient electronic interaction between Ru and Co atoms in the Co-Ru alloy, leading Ru to bear a negative charge. Fig. 2c showed the Co 2p high resolution spectra for Co/CQDs and $CoRu_{0.5}$/CQDs. The binding energy (BE) of Co/CQDs at 781.5 and 785.3eV are ascribed to Co $2p_{1/2}$ of Co^0 and Co^{2+}, while the high BEs at 788.5 and 797.5 eV are attributed to Co 2p3/2 of Co^0 and Co^{2+}, respectively. The concomitant satellite peaks are at the BEs of 788.5 (Co $2p_{1/2}$) and 803.4 eV (Co $2p_{3/2}$). The Ru 3p high resolution peak of Ru/CQDs and $CoRu_{0.5}$/CQDs were shown in Fig. 2d. The BE of Ru/CQDs at 462.8 and 485.1 eV are attributed to metallic Ru $3p_{3/2}$ and Ru $3p_{1/2}$. The Ru 3p binding energy of $CoRu_{0.5}$/CQDs has a weak shift to the low BE about 0.5 eV, while the Co 2p spectra of $CoRu_{0.5}$/CQDs are slightly shifted to the high BE direction, implying that there is an electronic interaction between Ru and Co in the CoRu nanoalloy. This also suggests that the electrons may transfer from Co to Ru via efficient electronic coupling between them, leading to a electron-rich Ru.

To understand the local electronic and atomic arrangement of the $CoRu_{0.5}$/CQDs

at the atomic level, X-ray absorption near-edge structure (XANES) and Fourier transform extended X-ray absorption fine structure (FT-EXAFS) measurements were conducted selectively measured at Co K-edge. From the XANES spectra of Co K-edge in Fig. 2e, we found that the absorption edge energies of Co K-edge in the $CoRu_{0.5}$/CQDs were lower than that in CoO, but higher than that in Co foil, which indicated that average value states of Co element in the $CoRu_{0.5}$/CQDs was less than +2. In order to further investigate the interaction between Ru and Co, Fourier transform (FT) EXAFS analysis was performed at Co K-edge (Fig. 2f). In FT-EXAFS curves of Co K-edge (Fig. 2f), Co-O coordination was not observed and the peak at 2.4Å results from Co–Ru interaction. It is necessary to mention that the position of Co–Ru peaks is obviously positive than that of Co–Co in Co foil (2.16 Å). This result confirmed that Co-Ru bonds could be formed after incorporation of Ru into the Co lattice, on the other hand, the higher lengths position of Co–Ru peaks respect to the Co foil peak at 2.16 Å can also be attributed to the geometrical effect by Ru atom. It was further proved that the lattice parameters of CoRu nanoalloy had changed by introducing the Ru atom.

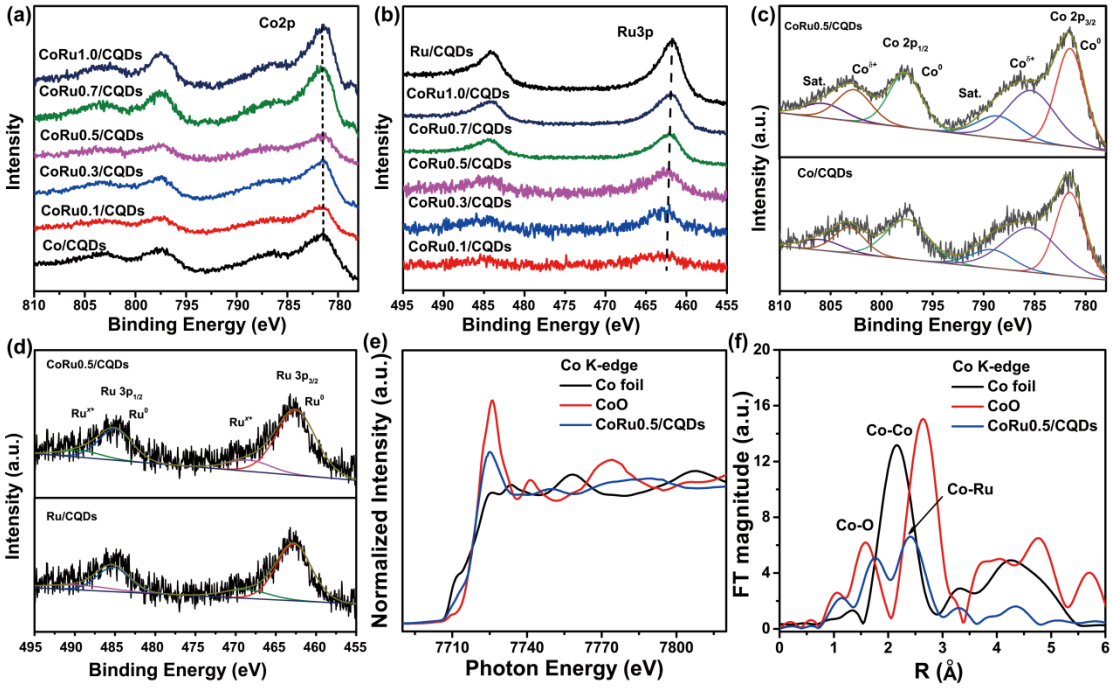

Fig. 2 a) Comparing the Co 2p core-level XPS spectrum of $CoRu_x$/CQDs with that of Co/CQDs. b) Comparing the Ru 3p core-level XPS spectrum of $CoRu_x$/CQDs with that of Ru/CQDs. High-resolution XPS spectra of $CoRu_{0.5}$/CQDs for c) Co 2p and d) Ru 3p, e) XANES spectra of $CoRu_{0.5}$/CQDs for Co K-edge, f) Fourier transformed (FT) EXAFS spectra of $CoRu_{0.5}$/CQDs for Co K-edge.

The hydrogen evolution reaction (HER) catalytic performance was tested on a GCE using a three-electrode system in 1.0 M KOH solution. The polarization curves without iR correction were obtained by linear sweep voltammetry (LSV) with a sweep rate of 5 mV s^{-1}. The loading of the catalyst is 0.42 mg cm^{-2}. The HER performance was evaluated by the overpotential with respect to the reversible hydrogen electrode (RHE) at 10 mA cm^{-2}, which is the current density expected for a 12.3% efficient solar water-splitting device.

For comparison, the electrocatalytic activities of Co/CQDs, Ru/CQDs, and 20 wt% commercial Pt/C were also investigated under the same conditions. As revealed in Fig. 3a, the pure Co/CQDs catalyst showed poor HER activity while CoRu0.5/CQDs exhibited excellent HER catalytic activity with near-zero onset overpotential. Importantly, $CoRu_{0.5}$/CQDs required an overpotential of about 18 mV at a current density of 10 mA cm^{-2}, which is 12 mV lower than that of commercial Pt/C (30 mV). However, Ru/CQDs (η = 88 mV @10 mA cm^{-2}) exhibited slightly lower HER activity. As shown in Fig. 3b, the overpotentials of $CoRu_x$/CQDs followed a valley trend with the increasing Ru content, where the $CoRu_{0.5}$/CQDs catalyst displayed the highest HER activity. The HER kinetics of the $CoRu_x$/CQDs were also calculated via corresponding Tafel plots. As shown in Fig. 3c, the Tafel slope of the $CoRu_{0.5}$/CQDs was 38.5 mV dec^{-1}, which is much smaller than that Pt/C (43.2 mV dec^{-1}) and other $CoRu_x$/CQDs samples, demonstrating a more efficient kinetics of hydrogen evolution. Electrochemical impedance spectra (EIS) were employed to study the interfacial electron transfer dynamics of the various catalysts, the related Nyquist plots and equivalent circuit were shown in Fig. S13. The Nyquist curves and the equivalent circuit indicates that $CoRu_{0.5}$/CQDs has much smaller Rct (6.8 Ω) than those of Pt/C and other control catalysts (Tab. S2). It suggested that $CoRu_{0.5}$/CQDs possesses the fastest charge transfer rate in the reaction kinetics at the interface of the catalyst and the electrolyte. We attribute the high efficiency to a synergic effect between the $CoRu_{0.5}$ alloy and the CQDs that help reduce the charge-transfer resistance at the catalyst/electrolyte interface, thus increasing the electrochemical conductivity. Furthermore, double-layer capacitance (C_{dl}) was identified as an important indicator for the effective electrochemically active surface area. The results in Fig. S14 revealed a larger C_{dl} of $CoRu_{0.5}$/CQDs (112.4 mF cm^{-2}) compared with that of other $CoRu_x$/CQDs samples, supporting more accessible active sites constructed on $CoRu_{0.5}$/CQDs. The long-term potential cycling performance was measured to evaluate the stability of $CoRu_{0.5}$/CQDs.

As shown in Fig. 2d, the $CoRu_{0.5}$/CQDs showed an insignificant (2 mV) loss in catalytic activity with a slight current deterioration before and after 5000 cyclic voltammetry (CV) cycles, indicating excellent electrochemical durability in 1 M KOH. In the durability cycle test, the chronoamperometry (i–t) curve of $CoRu_{0.5}$/CQDs (Fig. 2d, inset) showed nearly no significant decay after 100 h, suggested its robust cycling stability.

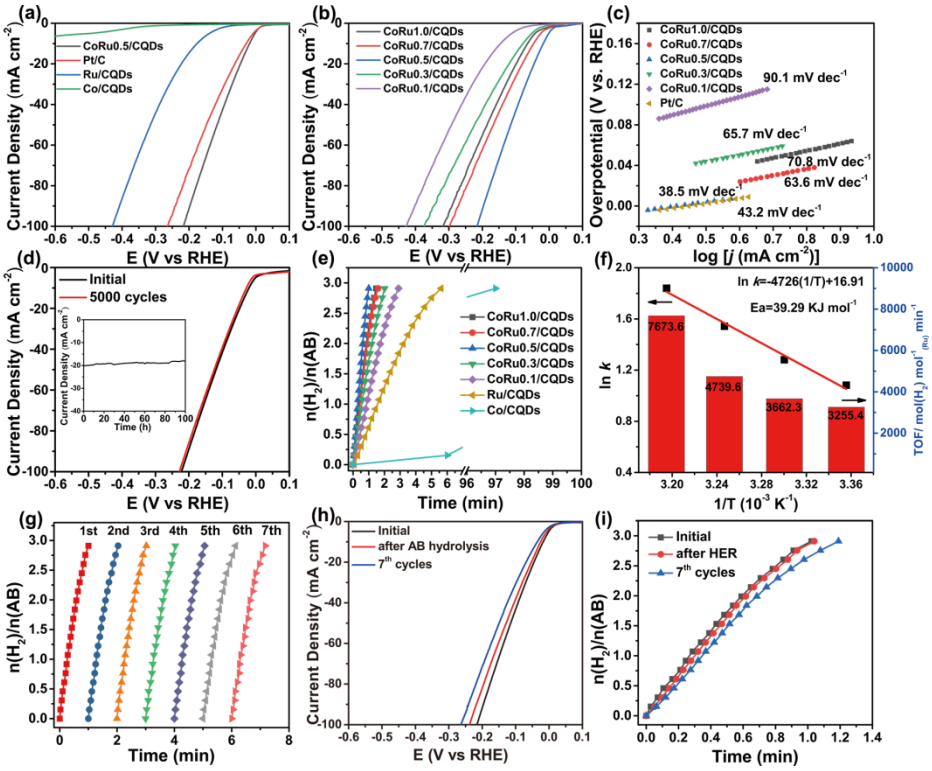

Fig. 3 a) HER polarization curves of $CoRu_{0.5}$/CQDs, Ru/CQDs, Co/CQDs and 20 wt% commercial Pt/C, b) HER polarization curves, c) Tafel plots of $CoRu_x$/CQDs and Pt/C, d) Polarization curves of $CoRu_{0.5}$/CQDs before and after 5000 CV cycles in 1 KOH (inset: Chronopotentiometry curves of $CoRu_{0.5}$/CQDs in 1 M KOH), e)Plots of time versus volume of hydrogen generated from aqueous AB catalyzed by $CoRu_x$/CQDs at 298 K (with 1.42 mmol AB and 10 mg catalyst in 10 mL water at 298 K), f) Arrhenius plots and TOF values of AB hydrolytic dehydrogenation catalyzed by CoRu0.5/CQDs at different temperatures, g) Durability test for hydrogen generation from AB aqueous solution (5 mL, 1.42 mmol) catalyzed by $CoRu_{0.5}$/CQDs at 298 K, h) Linear sweep voltammetry curves of $CoRu_{0.5}$/CQDs before and after hydrolysis of AB and after seven cycles in 1 M KOH; i) Catalytic performance of $CoRu_{0.5}$/CQDs for AB hydrolysis dehydrogenation before and after HER and after seven cycles.

The as-prepared $CoRu_x$/CQDs samples were also employed for AB hydrolysis to generate hydrogen at atmospheric pressure, compared with the Ru/CQDs and Co/CQDs

samples. As shown in Fig. 3e, the Co/CQDs showed almost no catalytic activity, meanwhile, Ru/CQDs showed a poor activity, with 95 mL of H_2 generated within 6 min. The $CoRu_{0.5}$/CQDs exhibited the highest activity, with which 95 mL H_2 could be released within only 0.99 min at room temperature which is greater than $CoRu_{1.0}$/CQDs (1.47min), $CoRu_{0.7}$/CQDs (1.59min), $CoRu_{0.3}$/CQDs (2.01min) and $CoRu_{0.1}$/CQDs (2.9min). This excellent catalytic activity could be attributed to the synergistic structural and electronic effects of $CoRu_{0.5}$/CQDs through the interaction of Co and Ru in relation to the so-called ligand and strain effects and the strong metal-support interaction of CoRu alloy with N-doping carbon layer. In order to obtain the activation energy (Ea) of the AB hydrolysis catalyzed by $CoRu_{0.5}$/CQDs, the hydrolytic reaction at different temperatures ranging from 298 K to 318 K were carried out (Fig. S15), and the rate constant (k) was determined from the nearly linear portion of the plot for each temperature. As shown in Fig. 3f, the hydrogen generation rate increases by increasing the reaction temperature as expected. The catalytic reactions for H_2 generation from AB were completed in 0.99, 0.89, 0.68 and 0.42 min at 298, 303, 308, and 313K, respectively, corresponding to TOF values of 3255.4, 3662.3, 4739.6, and 7673.6 mol(H_2) $mol^{-1}_{(Ru)}$ min^{-1} and 814.7, 837.9, 883.9, 951.8 mol (H_2) $mol^{-1}_{(cat)}$ min^{-1}. The TOF of 3255.4 min^{-1} at 298 K is among the higher values reported for catalysts of AB hydrolysis (Tab. S4) and is better than that of commercial Pt/C (449.6 mol(H_2) $mol^{-1}_{(Pt)}$ min^{-1}), (Fig. S16). Consequently, the E_a value was calculated to be 39.29 kJ mol^{-1} by fitting the Arrhenius plot of ln(k) against 1/T, indicating the kinetic superiority of $CoRu_{0.5}$/CQDs toward AB hydrolysis. Fig. S17 displayed the plots of hydrogen generation from AB hydrolysis versus time with different catalyst amount and AB concentrations over $CoRu_{0.5}$/CQDs. The hydrogen generation rate (HGR) was measured by fitting the first five time increments of the plot for each catalyst amount and AB concentration. The logarithmic plot of HGR versus catalyst amount and AB concentrations were illustrated in the inset of Fig. S18, respectively. The slope of 0.98 of ln (HGR) versus ln [catalyst amount] manifested that hydrogen evolution from aqueous AB decomposition over $CoRu_{0.5}$/CQDs could be explained as first-order correlation with catalyst amount. Nevertheless, the slope of 0.098 of ln (HGR) versus ln [AB] suggested that hydrogen production from aqueous AB decomposition over $CoRu_{0.5}$/CQDs was zero-order with AB concentration.

The stability of the catalyst is important for practical applications. The catalytic activity of $CoRu_{0.5}$/CQDs showed no significant decline even after 7 runs (Fig. 3g),

demonstrating that the $CoRu_{0.5}$/CQDs have robust durability toward the hydrolytic dehydrogenation of AB at room temperature.This structural stability allowed $CoRu_{0.5}$/CQDs to be used again for electro HER after AB hydrolysis. Therefore, we used another method to fabricate the working electrode to reach a high catalyst loading. And the optimal HER activity was observed with a mass loading of 2.0 mg cm^{-2} on the Ni foam substrate as the literature. As shown in Fig. S19 a, the $CoRu_{0.5}$/CQDs present a small overpotential of 16 mV to reach a current density of 10 mA cm^{-2} in 1 M KOH. As expected, they also showed excellent stability when loaded on the Ni foam substrate(Fig. S19 b). The performance of the catalyst for the HER before and after its use in the hydrolytic dehydrogenation of NH_3BH_3 was shown in Fig. 3 h. We defined one hydrolysis of AB reaction plus one electrolysis of water as a cycle. After seven cycles, the HER performance remained excellent. Furthermore, the catalytic performance of reused $CoRu_{0.5}$/CQDs for AB hydrolysis was evaluated before and after electro HER (Fig. 3i), it showed no significant decline after seven cycles. These results demonstrated that $CoRu_{0.5}$/CQDs are promising catalyst candidate for achieving efficient electrochemical and chemical hydrogen generation. It is thus unified catalysis for the electrolysis of water and the hydrolysis of AB that provides highly efficient and superstable hydrogen production.

The TEM image of $CoRu_{0.5}$/CQDs after 7 cycles was shown in Fig. S20 a, it can be seen that the nanoparticles still remained well-dispersed, indicating excellent stability. From the XRD pattern in Fig. S20 b, it can be seen that the diffraction peaks of $CoRu_{0.5}$/CQDs were unchanged before and after the 7 cycles, indicating that the chemical composition was the same with the initial. The XANES and EXAFS spectra of $CoRu_{0.5}$/CQDs before and after 7 cycles were shown in Fig. S21, the absorption peak position of Co before and after 7 cycles was consistent with that before the cycles, indicating that the chemical valence states of Co and Ru did not change after the cycles, which further indicated that the catalyst had good structural stability.

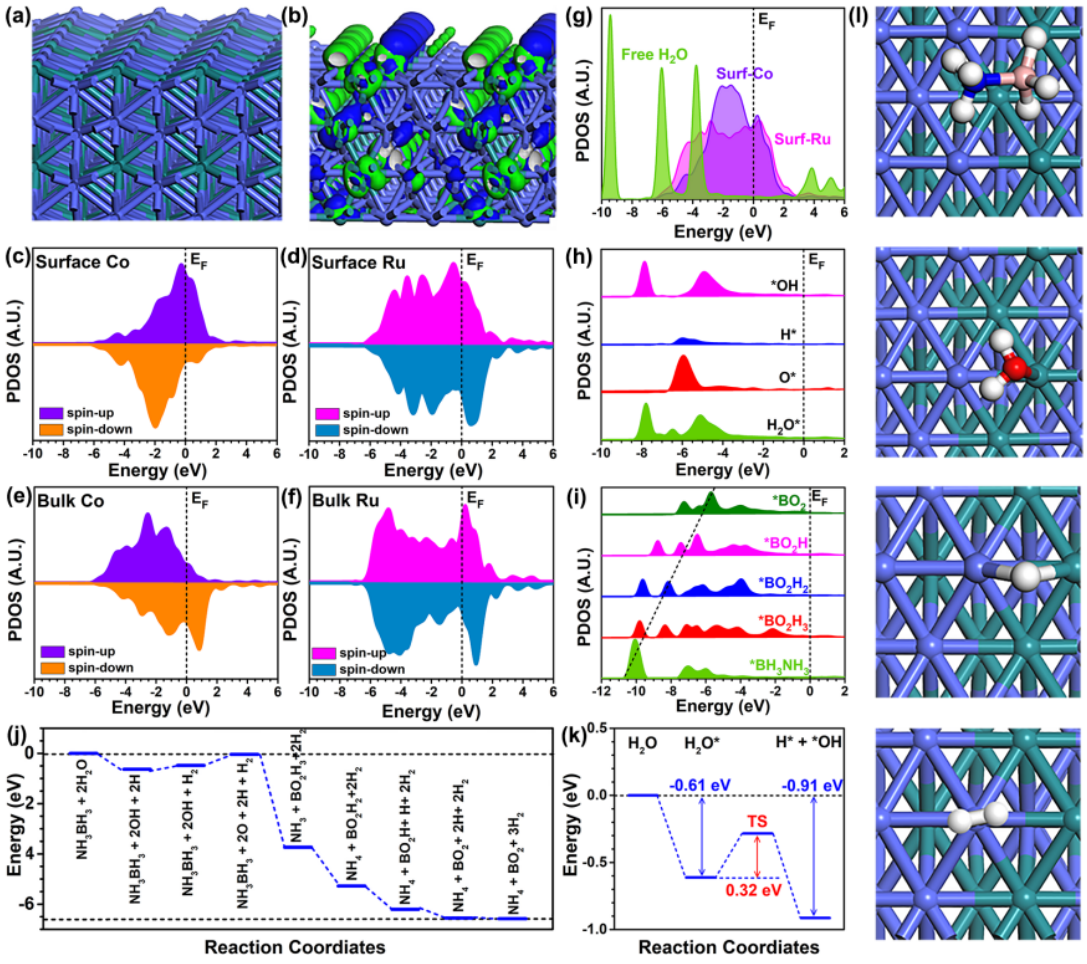

Fig. 4 a) The structure of $CoRu_{0.5}$/CQDs. Blue balls = Co and Green Balls= Ru. b) The real spatial contour plots for bonding and anti-bonding orbitals near E_F. The spin-polarized PDOS of c) Co-3d and d) Ru-4d on both surface $CoRu_{0.5}$/CQDs. The spin-polarized PDOS of e) Co-3d and f) Ru-4d on bulk CoRu0.5/CQDs. g) The PDOS of $CoRu_{0.5}$/CQDs surface with the H_2O adsorption. h) The PDOS of *s,p* orbitals of the intermediates during H_2O dissociation on the $CoRu_{0.5}$/CQDs surface. i) The PDOS of key intermediates during the hydrolysis of AB. j) The energy diagram of the AB hydrolysis. k) The energy diagram of water dissociation on $CoRu_{0.5}$/CQDs in the alkaline condition. l) The structural configuration of key species during the AB hydrolysis and HER process. Blue balls = Co, Green Balls= Ru, Dark balls = N, Pink balls = B, Red balls = O and White balls= H.

We have investigated the remarkable performance of HER by the electrocatalysis of AB on CoRu. The optimal $CoRu_{0.5}$ lattice has been constructed according to the experimental characterizations (Fig. 4a). The electronic orbital distribution shows that the electroactivity mainly locates on the surface Ru sites, which is playing a significant role in promoting the initial H_2O adsorption and dissociation (Fig. 4b). Then the projected partial density of states (PDOS) with spin-polarization is shown to examine the electronic structures of the surface and bulk of $CoRu_{0.5}$. For the surface, the Ru display a slightly lower d-band center and protects the valence of the Co sites, which preserves the appropriate H-binding strength without overbinding effect (Fig. 4c,d). In

comparison, the d-band centers of bulk Co and Ru both shift to the deeper position and become more electron-rich, supporting the electroactivity of bulk Co and Ru are obviously suppressed (Fig. 4e,f). Such an electronic environment exhibits the efficient electron-transfer route, in which the abundant bulk electrons deplete through the electroactive surface to the adsorbates for HER. The surface Ru and Co show relatively large overlap, confirming their couplings as identified by the experimental XPS results. For the free H_2O, it is noted that Ru sites show the larger overlapping than Co sites, which leads to the dominant role of Ru in the initial activation of H_2O on the surface (Fig. 4g). The further demonstrations of the PDOS of related species during the H_2O adsorption confirm that the important role of Ru in promoting the electron transfer (Fig. 4h). To guarantee the efficient AB hydrolysis for HER, the adsorptions of other intermediates are also crucial. Notably, a nearly linear correlation has been observed within the reaction coordinates, indicating an efficient electrocatalysis process achieved by the balance between adsorption and electron transfer. This also supports the electroactivity of $CoRu_{0.5}$ lattice has been well preserved, leading to an energetically favorable catalytic process for the main intermediates (Fig. 4i). Then, we move to study the HER process from an energetic perspective. We have devised the complex AB hydrolysis reaction pathway including $6e^-$ electron transfer based on the holistic consideration of the electronic structure of the $CoRu_{0.5}$ lattice. The reaction has shown an overall downhill trend for the generation of H_2, which is consistent with our electronic structure calculations. The only energy barrier is found at the dissociation of OH* to O*, which is the potential reaction determining step (RDS). This step requires 0.43 eV to overcome the barrier height. Moreover, the large energy drop of 3.69 eV for the dissociation of AB and the combination with O* is noted, which illustrates the binding trend of B-O is much larger than the B-OH. Such an evident binding contrast result in the proposed reaction pathway (Fig. 4j). Meanwhile, the energy diagram of the initial H_2O dissociation supports the activation of H_2O on is preferred from the energetic view. The energy barrier of 0.32 eV for the transient state (TS) is smaller than that of the RDS, guarantees the express H_2O dissociation during HER (Fig. 4k). The structural configurations confirm the stable adsorption of AB and H_2O near the Ru sites. The desorption of H_2 occurs near the Co sites (Fig. 4l). Therefore, the introduction of the appropriate Ru to Co improves the electroactivity to initiate the water dissociation in the alkaline condition and balance the H strength to facilitate the efficient HER.

Conclusion

In summary, we successfully synthesized the $CoRu_x$ nanoalloy ($CoRu_x$/CQDs) catalysts with the Ru modified lattice strain. The proper component ratio, the effective electronic coupling of Co and Ru, and strain effect, which lead to the faster interfacial electron transfer dynamics thus improving the catalytic performance. The resulting $CoRu_{0.5}$/CQDs not only exhibited extraordinary catalytic activity for HER in 1M KOH (η = 18 mV @ 10 mA cm^{-2}) but also shows outstanding activity for chemical hydrogen generation from the hydrolysis of ammonia borane (AB) with a high turnover frequency (TOF) of 3255.4 mol(H_2) $mol^{-1}_{(Ru)}$ min^{-1} and 814.7 mol (H_2) $mol^{-1}_{(cat)}$ min^{-1} at 298 K, respectively, representing the top level among the state-of-the-art catalysts. X-ray absorption spectroscopy and DFT calculations both confirm the modified electronic structures of the catalyst induced by the Ru incorporation, which achieves the balance between the electroactivity and the suitable adsorption strength to guarantee the efficient hydrogen generation. Furthermore, the $CoRu_{0.5}$/CQDs shows excellent cycle stability for HER and the hydrolysis of AB after alternating 7 cycles, which indicates a great potential of the catalyst in realizing the efficient hydrogen generation in future practical applications. Our work supplies a new avenue for hydrogen production based on the facile transitional metal alloy with carbon quantum dots, which offers valuable references for advanced catalyst design.